Nanoscale Advances

ROYAL SOCIETY OF CHEMISTRY

PAPER

View Article Online
View Journal | View Issue

Cite this: *Nanoscale Adv.*, 2021, **3**, 3860

Diatomite waste derived N-doped porous carbon for applications in the oxygen reduction reaction and supercapacitors†

Youguo Huang, Yiyan Wang, Yezheng Cai, * Hongqiang Wang, Qingyu Li, Qiang Wu, Kui Liu and Zhaoling Ma *

Biomass waste recycling and utilization is of great significance for improving ecological environments and relieving the current energy crisis. Waste diatomite with an adsorbed mass of yeast protein resulting from beer filtration is feasibly converted into N-doped porous carbon (NPC) *via* high temperature thermal treatment. The resulting NPC inherits the three-dimensional hierarchical structure of the diatomite, with a unique rich-pore feature composed of micro/meso/macropores, which is beneficial for high exposure of the electrocatalytic sites and ion transfer and diffusion. The NPC compounds with controllable nitrogen doping are used for the oxygen reduction reaction (ORR) and in a supercapacitor. NPC-2 exhibits a half-wave potential of 0.801 V comparable to that (0.812 V) of commercially available Pt/C in alkaline media, along with a good methanol tolerance capacity and long-term stability for the ORR. Furthermore, as an electrode material, a symmetric supercapacitor based on NPC-2 manifests an outstanding specific capacitance of 151.5 F g^{-1} at a current density of 1 A g^{-1} and a considerable capacitance retention of 90.5% after a cycling performance test of 10 000 cycles. The NPC-2 based symmetric SC delivered an energy density of 13.47 W h kg^{-1} at a power density of 400 W kg^{-1}. This work highlights the environmental significance of converting waste diatomite into metal-free ORR catalysts and electrode materials for energy conversion and storage technologies.

Received 21st January 2021
Accepted 12th May 2021

DOI: 10.1039/d1na00057h

rsc.li/nanoscale-advances

1. Introduction

Developing renewable energy conversion and storage technologies is central to alleviating increasingly serious environmental and energy issues. Owing to the merits of the high energy conversion efficiency and eco-friendliness, fuel cells and metal–air batteries are thought to be promising alternatives to conventional fossil fuels.[1] However, the large-scale application of energy conversion devices is greatly restricted owing to the lack of economically viable and efficient catalysts for accelerating the intrinsically slow oxygen reduction reaction (ORR) at the cathode of these devices, which is generally catalyzed using platinum (Pt) (which is a scarce resource, known to have a high cost) in practical applications.[2,3] Searching for Pt-free transition metals and metal-free catalysts that enable efficient ORR catalysis represents the only way to overcome this obstacle. Supercapacitors (SCs), with the advantages of a high power density, a rapid charge–discharge capacity, and long lifespan, are promising energy storage devices for electric vehicles and portable electronics.[4] However, the energy density of SCs needs to be increased further by exploiting high performance electrode materials based on the energy equation $E = 1/2CV^2$, in which C is the specific capacitance and V represents the working potential of the supercapacitor (SC).

Thanks to the low cost, good resistance to impurities, and favorable adsorption superiorities for oxygen-containing species, owing to the tuned electron donor–acceptor properties between the heteroatoms and adjacent C atoms, heteroatom-doped carbon materials manifest a significant potential in oxygen electrocatalysis and energy storage areas.[5,6] It should be noted that N-doping represents a powerful strategy, when compared with other non-metallic heteroatom doping methods, for boosting the ORR catalytic capacity by creating active sites, and hydrophilic and adsorption properties.[7–9] Importantly, the considered construction of hierarchical carbon with a unique pore size distribution can promote exposure of the active sites and benefit ion transfer and diffusion, leading to an enhanced catalytic capability and specific capacitance.[10,11] Diatomite, mainly composed of amorphous $SiO_2 \cdot nH_2O$ and having a hierarchical porous structure, has been widely used as an adsorbent for food purification, as a catalytic carrier in the energy area and, importantly, as a template for constructing a three-dimensional porous structure.[12] Specifically, diatomite is widely applied in breweries for purifying beer by physically

Guangxi Key Laboratory of Low Carbon Energy Materials, School of Chemistry and Pharmaceutical Sciences, Guangxi Normal University, Guilin, China. E-mail: 18810629627@163.com; zhaolingma@163.com

† Electronic supplementary information (ESI) available. See DOI: 10.1039/d1na00057h

adsorbing beer yeast residues and metal impurities. The simple burial of the diatomite waste produced seriously damages the environment.[13] On the other hand, beer yeast contains a considerable portion of protein, which can be used as a carbon and nitrogen source. Reforming diatomite waste into low-cost N-doped porous carbon is considered to be a highly desirable strategy, which not only relieves the catastrophic environmental issues, but also affords additional economic value.

Herein, by exploiting diatomite waste comprised of yeast proteins as the precursor and dicyandiamide as the nitrogen source, N-doped porous carbons (NPCs) with different nitrogen contents were obtained by multistep carbonization. The resulting NPCs, with unique hierarchical porous features, were used as metal-free electrocatalysts in the ORR and as an electrode material in a supercapacitor (SC), and exhibited comparable performances. The optimal NPC-2 exhibited a decent catalytic activity, an efficient quasi-four electron pathway for the ORR, a high methanol tolerance, and an excellent long-time stability in alkaline media in contrast to the commercial Pt/C catalyst. Meanwhile, when used as a SC electrode material, the symmetric SC based on NPC-2 possessed a high specific capacitance, good rate performance, and excellent cycling stability in alkaline aqueous solution.

2. Experimental section

Dicyandiamide and hydrofluoric acid (HF) were purchased from Beijing Chemical Factory of China. Deionized water (H_2O) was produced in the lab using a water purifier.

2.1 Synthesis of NPCs

The synthesis of the NPCs was achieved using a two-step high temperature treatment at 250 and 800 °C, respectively, for 3 h. Diatomite waste was provided by Guilin Liquan Beer Co. Ltd. Dicyandiamide, as the nitrogen source, was decomposed and synchronously released NH_3. The operations are detailed below. The diatomite waste was first cleaned using H_2O and dried at 80 °C overnight. Then, dicyandiamide and waste diatomite, with a mass ratio of 2 : 1, were well mixed in 500 mL H_2O by magnetic stirring for 12 h. Next, the mixed solution was filtered and dried. The dried mixture was then preliminarily heated to 250 °C and kept at this temperature for 3 h with a heating rate of 3 °C min^{-1} under an N_2 atmosphere. Hereafter, the dried mixture was further heated to 800 °C at a heating rate of 5 °C min^{-1} for 3 h under N_2. The obtained annealed sample was subsequently etched with 20 wt% HF solution to remove the diatomite, washed with H_2O, and dried to obtain N-doped porous carbon (NPC-2, also abbreviated as NPC). NPC-1 and NPC-3 were also prepared using a similar method to NPC-2, except for a difference in the mass ratio of dicyandiamide and dried diatomite waste. As a reference, porous carbon (PC) was prepared using a procedure similar to that used for the N-doped porous carbon (NPC) except for the addition of dicyandiamide.

2.2 Characterizations

The morphological features of the as-prepared samples were characterized using scanning electron microscopy (SEM; Quanta 200 FEG, FEI, America) and transmission electron microscopy (TEM; 200 kV, JEM-100X II, Japan). The specific surface area was analyzed using Brunauer–Emmett–Teller (BET) analysis, and the pore volume and the pore size distribution were calculated using density functional theory (DFT) on a micromeritics instrument (JWBK; 122 W). The degree of defects was measured using Raman spectroscopy (Renishaw in Via). The element valence and element content are displayed through X-ray photoelectron spectra (XPS, XSAM-800, Al Kα, 15 kV).

2.3 Electrochemical measurements

2.3.1 Electrochemical measurements for the ORR. The ORR measurements were performed on electrochemical stations (CHI 760e) in O_2-saturated 0.1 M KOH aqueous solution in a three electrode system. The saturated calomel electrode (SCE), graphite rod, and catalyst-coated glassy rotating disk electrode (RDE, diameter 5 mm) served as the reference electrode, counter electrode and working electrode, respectively. For catalytic ink preparation, 1 mg of the active material or 20 wt% Pt/C commercial catalyst were well distributed into a mixed solution containing 480 μL deionized water, 500 μL ethanol, and 20 μL Nafion solution (5 wt%) using sonication. Then, 20 μL of the obtained catalytic ink was dropped onto the surface of the glassy carbon electrode and dried in air.

Linear sweep voltammetry (LSV) was recorded at different rotating speeds from 400 to 1600 rpm at a voltage range of 0.2–1.0 V with a scan speed of 10 mV s^{-1}. Cyclic voltammetry (CV) curves were recorded in a voltage range of −0.2–1.0 V with a scan speed of 50 mV s^{-1}.

The catalytic stability and methanol-tolerance measurements were carried out using a chronoamperometry measurement at 1600 rpm and the potential was controlled at 0.7 V under a continuous O_2 supply. The electron transfer number (n) was calculated according to the Koutecky–Levich equations:

$$1/j = 1/j_k + 1/(B\omega^{1/2}) \quad (1)$$

$$B = 0.2nFC_0D_0^{2/3}V^{-1/6} \quad (2)$$

in which, j is the measured current density, j_k is the kinetic-limiting current density, ω is the electrode rotating speed in rpm, n is the electron transfer number for the ORR process, F is the Faraday constant, which is about 96 485 C mol^{-1}, C_0 is the solubility of O_2 in 0.1 M KOH of about 1.2×10^{-6} mol cm^{-3}, D_0 is the O_2 diffusion coefficient in 0.1 M KOH, which is about 1.9×10^{-5} cm^2 s^{-1}, and V is the kinematic viscosity, which is about 0.01 cm^2 s^{-1}.

The rotating ring disk electrode (RRDE) measurement was carried out under O_2 saturated 0.1 M KOH aqueous solution at a rotation speed of 1600 rpm and the ring potential was set at 1.3 V. The electron transfer number (n) and hydrogen peroxide yield (H_2O_2) were analyzed based on the following equations:

$$n = 4I_d/(I_d + I_r/N) \quad (3)$$

$$HO_2^- = (200I_r/N)/(I_d + I_r/N) \quad (4)$$

in which, I_r and I_d are the ring current (A) and the disk current (A), and N is the collecting current efficiency (0.37) of the platinum ring.

2.3.2 Electrochemical measurements for the SC. The electrodes used for the SCs were prepared by mixing the NPC, carbon black, and binder (PTFE) well, at a mass ratio of 8 : 1 : 1. The obtained mixture was pressed into an electrode sheet and subsequently punched into electrode discs (d = 12 mm), followed by drying in a vacuum oven. To construct a SC (2025 coin type cell), two pieces of the electrode sheets with an equivalent mass were assembled by using cellulose paper as a separator and 6 M KOH alkaline solution as an electrolyte.

The electrochemical measurements for the SC were performed on CHI660E electrochemical stations (Shanghai Chenhua Instruments Co. China). CV and galvanostatic charge–discharge (GCD) curves were both measured in the potential range of 0–1 V respectively, at a scan rate range of 10 to 200 mV s^{-1} and current densities of 1 to 5 A g^{-1}. Electrochemical impedance spectroscopy (EIS) studies were taken in the frequency range of 100–0.001 kHz with a voltage amplitude of 5 mV. The long-term cycling stability was evaluated on a land cell test system. The specific capacitance of a SC can be calculated from the GCD curves according to the following equations:

$$C = 2I \times \Delta t/(m \times \Delta V) \quad (5)$$

$$E = 1/2 \times 1/3.6 \times C \times (\Delta V)^2 \quad (6)$$

$$P = 3600 \times E/\Delta t \quad (7)$$

in which, C is the specific capacitance (F g^{-1}), and I (A), Δt (s), m (g), ΔV (V), E (W h g^{-1}), and P (W kg^{-1}) represent the discharge current, discharge time, mass of active materials, potential, energy density and power density, respectively.

3. Results and discussion

The NPC was prepared by annealing the precursor mixture of diatomite waste and dicyandiamide as the carbon source and nitrogen source, respectively. The diatomite waste adsorbs yeast proteins during the beer filtration process. The digital photograph (Fig. 1A) and SEM image (Fig. 1B) of diatomite waste display rich-hole features with particulate and flake impurities, belonging to the yeast protein adsorbed within the hierarchical diatomite. Once subjected to high temperature treatment, the yeast protein was carbonized and the derived carbon was *in situ*

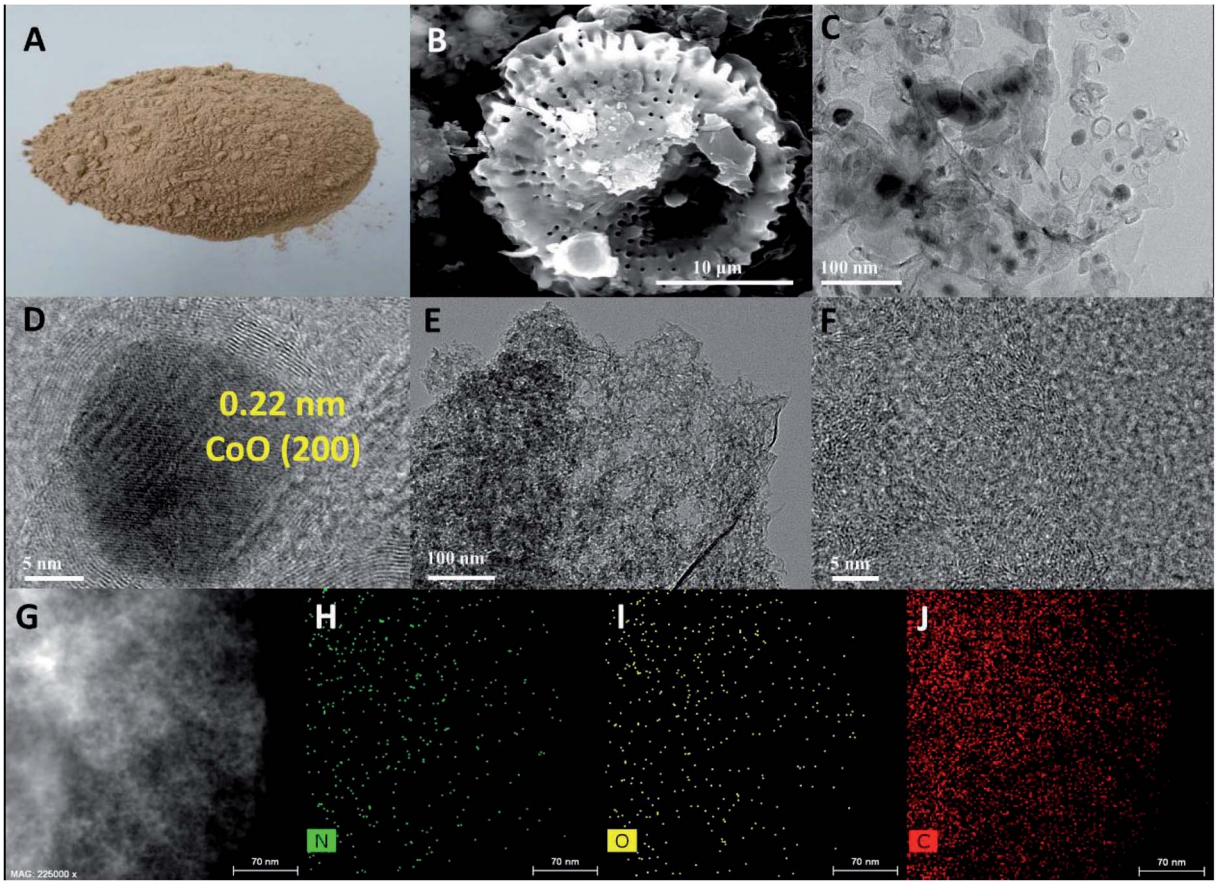

Fig. 1 Digital photograph (A) and SEM image (B) of the dried diatomite waste; TEM and HRTEM images of PC (C) and (D), and NPC-2 (E) and (F); and HRTEM images and the corresponding elemental mappings of NPC-2 (G)–(J).

coated on the surface of the diatomite. After the etching treatment, the diatomite template was removed, leading to the formation of a porous carbon structure inherited from the diatomite, as confirmed from the SEM image (Fig. S1A†) of PC. By introducing a suitable dicyandiamide while building the PC, we can obtain N-doping PC (marked as NPC-*X*, $X = 1$, 2, and 3) with a unique pore-rich feature mainly containing micro/meso/macropores, as evidenced from the formation of a loose configuration in the SEM images (Fig. S1B–D†) of NPC-1, NPC-2, and NPC-3. The loose structure with rich-pore features can be seen in NPC-1 with a low content of dicyandiamide, and NPC-3 displayed more abundant loose particles on the surface of the carbon framework. Considering that excessive loose particles are unfavorable for electro transfer, the amount of dicyandiamide introduced should be carefully optimized. TEM characterization (Fig. 1C) of the PC reveals the transparent nanosheets feature carbon with clear holes. It should be noted that some opaque black particles, which can be attributed to SiO_x or metal species, still exist on the surface of the PC and may benefit carbon graphitization, as evidenced from the clear lattice fringes of carbon (Fig. 1D). No identifiable particles can be seen in the overall microtopography of the NPC. TEM image of Fig. 1E indicates that N-doping can accelerate the removal of SiO_x and metal species, leading to the enhanced exposure of the pore structure. In addition, no clear lattice fringes can be seen in the high-resolution TEM (HRTEM) of the NPC (Fig. 1F), indicating an amorphous structure as the result of nitrogen doping. An additional HRTEM image and the corresponding elemental mapping distributions of the NPC reveal N, O, and C were evenly distributed in NPC-2 (Fig. 1G–J).

To reveal the crystal structure characteristics of the as-prepared samples, PC and NPC-2 were investigated using X-ray diffractometry (XRD). As shown in Fig. 2A, two diffraction peaks located at 26° and 43°, which are attributed to the (002) and (100) lattice faces of graphitic carbon, respectively, can be clearly observed for the PC. However, only a broader diffraction peak with a low intensity at about 25° can be observed for the NPC, indicating the obvious change in the crystal structure, which is the result of N-doping that reduces the degree of graphitization by increasing the number of defects and pores.[14] Raman spectra (Fig. 2B) of NPC and PC further confirm the lower degree of graphitization of NPC with much higher I_D/I_G values, compared to PC, which is consistent with the XRD results. The specific surface areas and pore structure characteristics of the samples were further examined by carrying out N_2 adsorption–desorption measurements. The N_2 adsorption–desorption isotherms (Fig. 2C) of PC and NPC show typical IV isotherms with a clear H4 type hysteresis loop. The pore size distributions (Fig. 2D) directly indicate the existence of a large number of micro/meso/macropores for NPC and that only mesopores can be detected for the PC.[15,16] The wide range of pore size distributions for the NPC further confirms the formation of a hierarchical structure. This different pore structure indicates that NPC (754 $m^2\ g^{-1}$) has a higher specific surface area than PC (658 $m^2\ g^{-1}$). Meanwhile, NPC (7.216 nm) manifests a relatively higher average pore diameter than PC (2.832 nm). Compared with PC, the additional generation of mesopores and macropores in NPC, originating from the de-templating and N-doping processes, improves the mass transfer and the ion transfer is significant for enhancing the catalysis of the ORR. The N_2 adsorption–desorption isotherms and pore structure characteristics of the NPC-1 and NPC-3 catalysts provided in Fig. S2† reveal the existence of microporous and mesoporous structures.

The surface compositions and valence states of the samples were measured using XPS and the results are listed in Table S1.† The XPS survey spectra (Fig. S3A†) show the coexistence of C, N, and O for the NPC samples, verifying that the nitrogen species have been incorporated into the carbon structure (Fig. S3B†). The high-resolution C 1s spectrum (Fig. 2E and G) of PC and NPC reveals the formation of C–N (286.1 eV) and C═N (289.5 eV), once again confirming the successful doping of the N atom

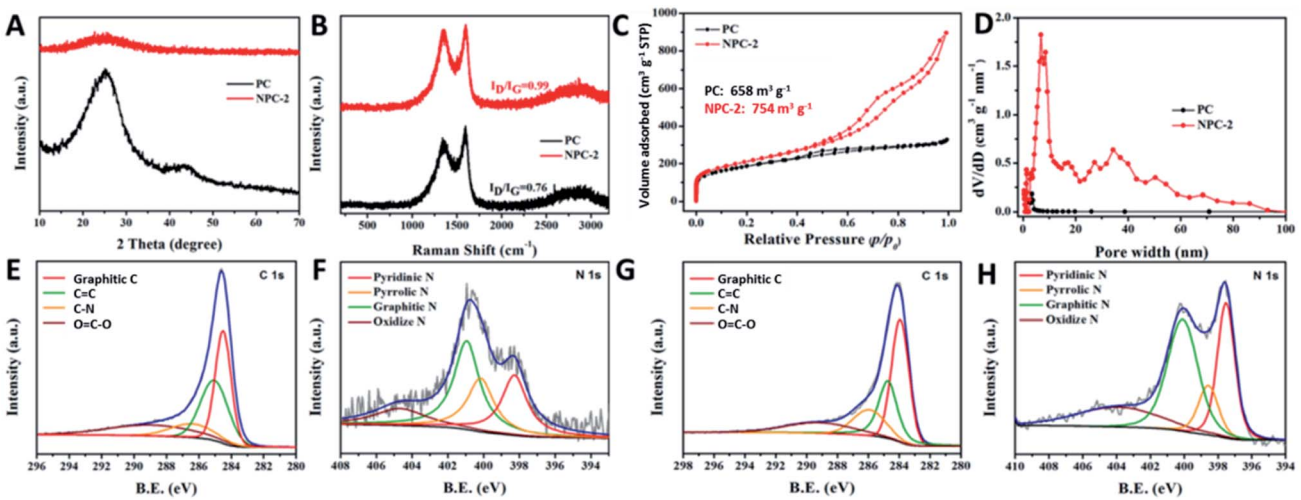

Fig. 2 XRD patterns (A), Raman spectra (B), nitrogen adsorption–desorption isotherm (C), and the pore size distribution curves (D) for PC and NPC-2. High-resolution C 1s and N 1s spectra of PC (E) and (F), and NPC-2 (G) and (H).

within the carbon matrix.[17] The N 1s spectrum (Fig. 2F and H) of PC and NPC, which can be divided into three peaks of pyridinic N (397.6 eV), pyrrolic N (398.6 eV), graphitic N (400.1 eV), and the π–π* satellite (404.0 eV), demonstrates the high content of pyridinic and graphitic N species, which are beneficial for improving the electronic conductivity, electrochemical capacitance, and ORR catalytic capacity.[18]

Encouraged by the unique architecture with pore-rich hierarchical features, the ORR performance of NPC was evaluated and compared with that for PC and the commercial Pt/C catalyst using CV and LSV methods in N_2 or O_2-saturated KOH aqueous solution (0.1 M). The CV curves recorded in the N_2-saturated KOH solution (Fig. 3A) show no oxygen reduction peak, but visible reduction peaks can be seen in the O_2-saturated KOH solution, suggesting active ORR catalysis for both PC and NPC. In addition, NPC presents a more positive potential of 0.815 V compared to PC (0.772 V), indicating a higher ORR catalytic activity. LSV curves (Fig. 3B) and the corresponding Tafel plots (Fig. 3C) confirm the enhanced ORR catalytic capacity of NPC, as evidenced from the significantly higher half-wave potentials ($E_{1/2}$) of NPC (0.801 V), which are comparable to those of the commercial Pt/C catalyst, compared to PC (0.719 V). Furthermore, NPC (0.891 V) also manifests a clearly higher onset potential for the ORR than that of PC (0.839 V), indicating improved ORR catalysis. The ORR catalysis of NPC-1 and NPC-3 were also evaluated as shown in Fig. S4.† The LSV curves of NPC-1 and NPC-3 with a relatively low limiting diffusion current density indicate a poor catalytic activity. In order to understand the dynamics of catalysis, the LSV curves (Fig. S5†) of NPC-2 at different rotation rates were recorded and the K–L plots are displayed in Fig. 3D; the inset in Fig. 3C shows a histogram of the electron transfer number (n). The calculated electron transfer number (n) of the NPC indicates the efficient quasi-four electron pathway for the ORR, similar to that of Pt/C.[19] To reveal the reaction mechanism, the RRDE measurements (Fig. S6†) were carried out on NPC-2 and commercial Pt/C, and the electron transfer number (n) values and H_2O_2 yield are displayed in Fig. 3E. RRDE curves were recorded in O_2-saturated 0.1 M KOH alkaline solution at 10 mV s^{-1} and a rotation speed of 1600 rpm, along with the ring electrode potential maintained at 1.3 V. The calculated n value for NPC-2 is 3.29–3.51 and 3.95–3.97 for Pt/C. The H_2O_2 yield of NPC-2 (23.78–35.72%) is higher than that of Pt/C (1.30–2.18%), signifying the coexistence of a two- and four-electron pathway for the ORR.

The methanol tolerance and stability are two key criteria for assessing the ORR performance of a catalyst. As shown in Fig. 3F, Pt/C suffered a sharp decrease in current owing to the methanol oxidation reaction after methanol (2 mL) was added into the KOH solution (100 mL). In contrast, the addition of methanol has no significant effect on NPC-2 for catalysis, and even a slightly increased current can be seen, demonstrating an excellent methanol resistance. The stability test (Fig. 3G) was performed using the chronoamperometry method and indicates that NPC-2 (86.8%) displays a relatively higher current retention compared to Pt/C (66.7%) after 20 000 s, suggesting an enhanced catalytic stability.[20,21] The catalytic stability of NPC-2 was also examined by consequent CV scanning of 5000 cycles. The LSV curve of the before and after 5000-cycle scans are provided in Fig. 3H. A slightly negative shift in $E_{1/2}$ after the stability test also confirms the good catalytic performance.

Considering the unique geometry and improved electronic structure, the as-prepared samples were also expected to show significant application potential in energy storage devices. As a probe, the electrochemical performance of the symmetric SC constructed using NPC-*X* samples as electrode materials was also evaluated. CV curves (Fig. S7†) of NPC-1, NPC-2, and NPC-3-based SCs manifest quasi-rectangular shape characteristics in the potential range of 0–1.0 V. In order to ensure the normal and

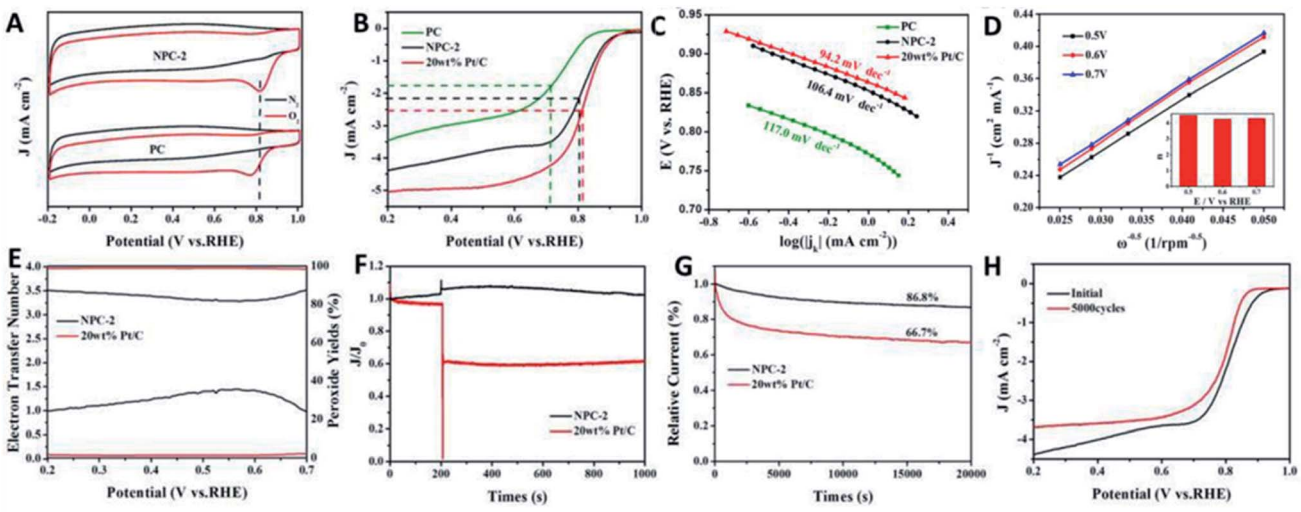

Fig. 3 ORR performance of the catalysts evaluated in 0.1 M KOH aqueous solution. (A) CV curves (50 mV s^{-1}) for N_2 and O_2-saturated PC and NPC-2; (B) and (C) LSV curves (10 mV s^{-1}) at 1600 rpm and the relevant Tafel plots for Pt/C and NPC; (D) Koutecky–Levich plots for NPC-2; (E)–(H) electronic transfer number and H_2O_2 yield (E), methanol-tolerance test (2 mL MeOH was added to the electrolyte) (F), I–t curves of PC and NPC-2 (G), and LSV curves of NPC-2 before and after 5000 potential cycles (H).

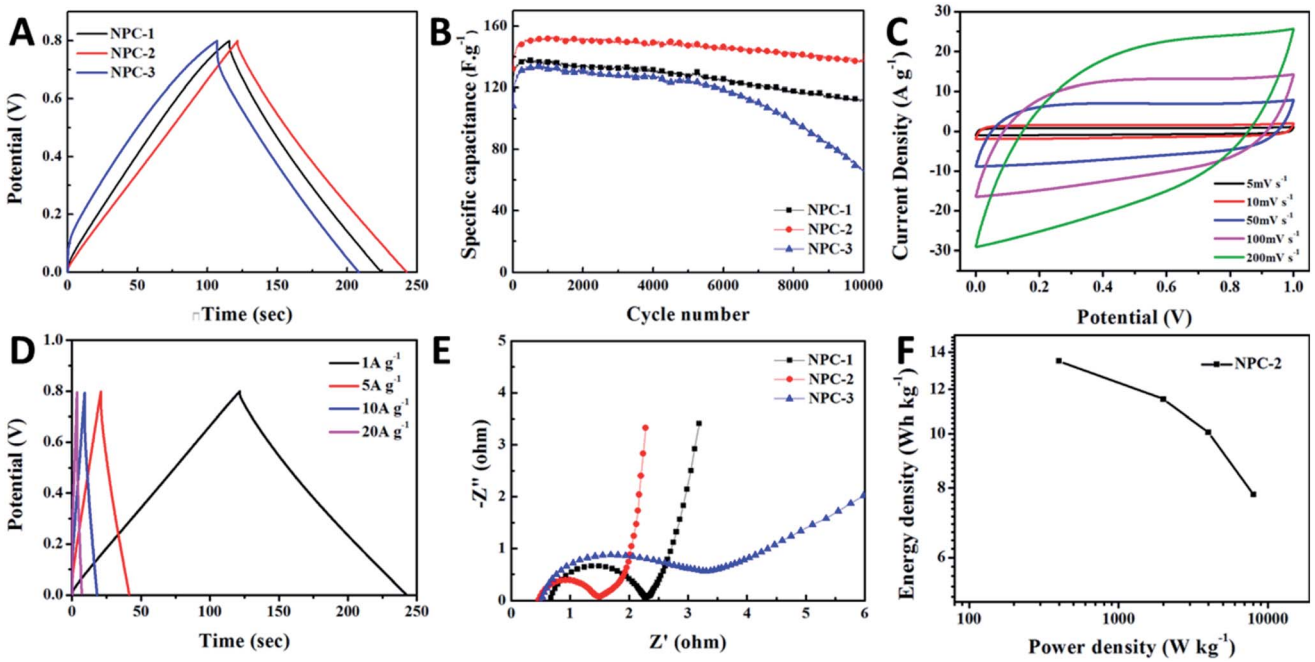

Fig. 4 Electrochemical performance of the SCs based on the NPC-*X* samples. (A) and (B) GCD curves and cycling performance (at 1 A g^{-1}) of NPC-1, NPC-2, and NPC-3; (C) and (D) CV curves of NPC-2 at different scanning rates and GCD curves at different current densities for the NPC-2-based SC; (E) Nyquist plots; and (F) Ragone plot of the energy density *versus* power density of the NPC-2-based SC.

efficient operation of the SC, the operating voltage range should be controlled at 0–0.8 V. The GCD curves are compared in Fig. 4A and show that NPC-2 has the longest discharge time, indicating the highest specific capacitance. The difference in the specific capacitance is the result of different microscopic geometries. Fig. 4B compares the cycling performance curves at a current density of 1 A g^{-1} for NPC-1, NPC-2, and NPC-3. Notably, NPC-2 possessed the highest specific capacitance among the tested samples and a high capacitance retention of 90.5%. The specific capacitance of NPC can be maintained at 142 F g^{-1}, even after a 10 000 cycle test. This can be attributed to the fact that NPC has rich adsorption sites for electronic movement benefiting from the layered porous carbon structure, high specific surface area, and doping of nitrogen, resulting in a higher specific capacitance. The CV curves (Fig. 4C) at different scan rates (from 5 to 200 mV s^{-1}) show an almost quasi-rectangular shape without redox peaks, even when the scan rate was raised to 200 mV s^{-1}. No obvious deformation can be observed, proving the good capacitance performance.[22–24] Fig. 4D displays the GCD curves at different current densities for NPC; the specific capacitances were calculated to be 151.5, 130, 112.5, 87.5 F g^{-1} at 1, 5, 10 and 20 A g^{-1}, respectively. This result is superior to common carbon materials, and a detailed comparison is provided in Table S2†.[25,26] This means the symmetrical SC based on NPC-2 is capable of achieving a fast charge–discharge capability. To further study the ion and electron transfer kinetics of the NPC, EIS measurements were carried out. The Nyquist plots in Fig. 4E indicate that NPC has the smallest interfacial resistance and charge transfer resistance and a fast ion diffusion rate. This result indicates the significance of the level of N-doping for tuning the electronic conductivity and electron kinetics.[27–29] Moreover, the relationship between the energy density and power density, as shown in the Ragone plot (Fig. 4F), indicates that NPC-2-based SC exhibited a high energy density of 13.47 W h kg^{-1} at a power density of 400 W kg^{-1}, comparable or superior to some reported carbon-based SCs.[30–34]

4. Conclusions

In summary, this work demonstrates a feasible strategy for the conversion of waste diatomite into a metal-free, N-doping, and hierarchical mesoporous structured carbon for ORR catalysis and energy storage in SCs. As a catalyst, the as-prepared NPC-2 delivered a half-wave potential comparable to that of commercially available Pt/C in alkaline medium and manifested an improved methanol tolerance capacity and long-term stability compared to the latter. When used as an electrode material, a symmetrical SC based on NPC-2 was found to possess a relatively high specific capacitance of 151.5 F g^{-1} at a current density of 1 A g^{-1} and an excellent cycling performance, with a 90.5% initial specific capacitance retention after 10 000 cycles. The NPC-2-based symmetric SC delivered an energy density of 13.47 W h kg^{-1} at a power density of 400 W kg^{-1}. The outstanding electrochemical performance of NPC can be attributed to the unique rich-pore features composed of micro/meso/macropores. This work provides a feasible strategy for converting waste diatomite into metal-free ORR catalysts and electrode materials for energy conversion and storage technologies.

Conflicts of interest

There are no conflicts to declare.

Acknowledgements

This work was supported by the National Natural Science Foundation of China (22002025), the Guangxi Natural Science Foundation of China (2018GXNSFBA281123), the Special Fund for Guangxi Distinguished Expert, Guangxi Innovation Driven Development Subject (GUIKE AA19182020, GUIKE AA19254004, GUIKE AA18118005, GUIKE AD19110134), the Guangxi Technology Base and Talent Subject (GUIKE AD18126001), the Guangxi Youth promotion program (2019KY0073) and the Guangxi Normal University Natural Science Foundation of China (2017ZD006, 2018BQ009).

References

1 W. Sun, F. Wang, B. Zhang, M. Zhang, V. Küpers, X. Ji, C. Theile, P. Bieker, K. Xu, C. Wang and M. Winter, *Science*, 2021, **371**, 46–51.
2 J. Han, H. Bao, J.-Q. Wang, L. Zheng, S. Sun, Z. L. Wang and C. Sun, *Appl. Catal., B*, 2021, **280**, 119411–119420.
3 W. Li, D. D. Wang, Y. Q. Zhang, L. Tao, T. H. Wang, Y. Q. Zou, Y. Y. Wang, R. Chen and S. Y. Wang, *Adv. Mater.*, 2020, **32**, 1907879–1907898.
4 S. Kumar, G. Saeed, L. Zhu, K. N. Hui, N. H. Kim and J. H. Lee, *Chem. Eng. J.*, 2021, **403**, 126352–126369.
5 L. Zhou, P. Zhou, Y. Zhang, B. Liu, P. Gao and S. Guo, *J. Energy Chem.*, 2021, **55**, 355–360.
6 D. Banham, J. Y. Choi, T. Kishimoto and S. Ye, *Adv. Mater.*, 2019, **31**, 1804846–1804851.
7 C. Kim, C. Zhu, Y. Aoki and H. Habazaki, *Electrochim. Acta*, 2019, **314**, 173–187.
8 J. Wang, H. Li, S. Liu, Y. Hu, J. Zhang, M. Xia, Y. Hou, J. Tse, J. Zhang and Y. Zhao, *Angew. Chem., Int. Ed.*, 2021, **60**, 181–185.
9 J. Quílez-Bermejo, E. Morallón and D. Cazorla-Amorós, *Carbon*, 2020, **165**, 434–454.
10 L. Yang, J. Shui, L. Du, Y. Shao, J. Liu, L. Dai and Z. Hu, *Adv. Mater.*, 2019, **31**, 1804799–1804818.
11 B. Wei, H. Liang, Z. Qi, D. Zhang, H. Shen, W. Hu and Z. Wang, *Chem. Commun.*, 2019, **55**, 1402–1405.
12 J. Li, J. Xu, Z. Xie, X. Gao, J. Zhou, Y. Xiong, C. Chen, J. Zhang and Z. Liu, *Adv. Mater.*, 2018, **30**, 1800548–1800555.
13 Z. Ma, Z. Zhang, Y. Qu, F. Lai, Q. Li, X. Wu, Q. Wu, Q. Li, H. Wang and Y. Huang, *Microporous Mesoporous Mater.*, 2019, **281**, 50–56.
14 C. You, S. Liao, X. Qiao, X. Zeng, F. Liu, R. Zheng, H. Song, J. Zeng and Y. Li, *J. Mater. Chem. A*, 2014, **2**, 12240–12246.
15 Q. Wei, X. Yang, G. Zhang, D. Wang, L. Zuin, D. Banham, L. Yang, S. Ye, Y. Wang, M. Mohamedi and S. Sun, *Appl. Catal., B*, 2018, **237**, 85–93.
16 Y. Yang, M. Luo, Y. Xing, S. Wang, W. Zhang, F. Lv, Y. Li, Y. Zhang, W. Wang and S. Guo, *Adv. Mater.*, 2018, **30**, 1706085–1706092.
17 E. Hu, X.-Y. Yu, F. Chen, Y. Wu, Y. Hu and X. W. D. Lou, *Adv. Energy Mater.*, 2018, **8**, 1702476–1702483.
18 H. Yu, L. Shang, T. Bian, R. Shi, G. I. Waterhouse, Y. Zhao, C. Zhou, L. Z. Wu, C. H. Tung and T. Zhang, *Adv. Mater.*, 2016, **28**, 5080–5086.
19 M.-C. Liu, C. Lu, Y. Xu, Y.-X. Hu, J. Li, H. Zhang, Y.-S. Zhang, B.-M. Zhang, L.-B. Kong, W.-W. Liu, W.-J. Niu, K. Zhao, L. Lee, Z. M. Wang and Y.-L. Chueh, *ACS Sustainable Chem. Eng.*, 2019, **7**, 18690–18699.
20 J. Li, M. Chen, D. A. Cullen, S. Hwang, M. Wang, B. Li, K. Liu, S. Karakalos, M. Lucero, H. Zhang, C. Lei, H. Xu, G. E. Sterbinsky, Z. Feng, D. Su, K. L. More, G. Wang, Z. Wang and G. Wu, *Nat. Catal.*, 2018, **1**, 935–945.
21 L. An, N. Jiang, B. Li, S. Hua, Y. Fu, J. Liu, W. Hao, D. Xia and Z. Sun, *J. Mater. Chem. A*, 2018, **6**, 5962–5970.
22 J. Li, X. Li, D. Xiong, L. Wang and D. Li, *Appl. Surf. Sci.*, 2019, **475**, 285–293.
23 S. Kumar, I. A. Mir, L. Q. Xiao, L. Zhu and K. N. Hui, *J. Alloys Compd.*, 2021, **852**, 156764–156767.
24 X. Feng, J. Ning, M. Xia, H. Guo, Y. Zhou, D. Wang, J. Zhang and Y. Hao, *Nanotechnology*, 2021, **32**, 035402–035409.
25 P. Chang, H. Mei, Y. Zhao, W. Huang, S. Zhou and L. Cheng, *Adv. Funct. Mater.*, 2019, **29**, 1903588–1903600.
26 K. P. Annamalai, X. Zheng, J. Gao, T. Chen and Y. Tao, *Carbon*, 2019, **144**, 185–192.
27 B. A. Ali, A. M. A. Omar, A. S. G. Khalil and N. K. Allam, *ACS Appl. Mater. Interfaces*, 2019, **11**, 33955–33965.
28 B. Zhao, C. Song, F. Wang, W. Zi and H. Du, *Microporous Mesoporous Mater.*, 2020, **306**, 110483–110489.
29 Y. Wang, H. Wang, T. C. Zhang, S. Yuan and B. Liang, *J. Power Sources*, 2020, **472**, 228610–228617.
30 D. He, W. Zhao, P. Li, Z. Liu, H. Wu, L. Liu, K. Han, L. Liu, Q. Wan, F. K. Butt and X. Qu, *Appl. Surf. Sci.*, 2019, **465**, 303–312.
31 D. He, W. Zhao, P. Li, S. Sun, Q. Tan, K. Han, L. Liu, L. Liu and X. Qu, *J. Alloys Compd.*, 2019, **773**, 11–20.
32 M. Zhang, X. Jin, L. Wang, M. Sun, Y. Tang, Y. Chen, Y. Sun, X. Yang and P. Wan, *Appl. Surf. Sci.*, 2017, **411**, 251–260.
33 G. Lin, R. Ma, Y. Zhou, Q. Liu, X. Dong and J. Wang, *Electrochim. Acta*, 2018, **261**, 49–57.
34 G. Lin, R. Ma, Y. Zhou, C. Hu, M. Yang, Q. Liu, S. Kaskel and J. Wang, *J. Colloid Interface Sci.*, 2018, **527**, 230–240.